Corrosion Science 174 (2020) 108847

Contents lists available at ScienceDirect

Corrosion Science

journal homepage: www.elsevier.com/locate/corsci

Effect of grain ultra-refinement on corrosion behavior of ultra-high strength high nitrogen stainless steel

H. Zhang[a], P. Xue[a,*], L.H. Wu[a], Q.N. Song[b], D. Wang[a], B.L. Xiao[a], Z.Y. Ma[a,*]

[a] Shenyang National Laboratory for Materials Science, Institute of Metal Research, Chinese Academy of Sciences, 72 Wenhua Road, Shenyang, 110016, China
[b] College of Mechanical and Electrical Engineering, Hohai University, 200 Jinling North Road, Changzhou, 213022, China

ARTICLE INFO

Keywords:
Stainless steel
Scratching electrode
Potentiostatic
XPS
Repassivation

ABSTRACT

High-performance high nitrogen stainless steel (HNS) with ultra-high strength up to ~1.7 GPa and excellent corrosion resistance was successfully obtained by friction stir processing. The simultaneous enhancement in strength and corrosion resistance was mainly attributed to the grain ultra-refinement. Uniform ultrafine-grained microstructure (~225 nm) significantly improved the repassivation behavior of HNS. With significantly increased element diffusion rate and element content, the passive film formed on the ultrafine-grained HNS showed high resistance to the nucleation and growth of pits. Grain ultra-refinement was confirmed to be an effectual method for improving corrosion resistance of HNS without sacrificing strength.

1. Introduction

For the chemical industry, energy and marine engineering, stainless steels are one of the most important materials. High strength, high corrosion resistance and low-cost stainless steels are constantly developed. Among them, high nitrogen stainless steels (HNSs) have shown great advantages for their superior properties with the reduced content of expensive nickel element. Therefore, the HNSs have attracted massive attention [1–3].

The high nitrogen content of HNSs led to good work hardening ability. Ultra-high strength HNSs could be obtained by cold working [4,5]. However, with the increased amount of cold deformation, the corrosion resistance of the HNSs decreased sharply [3,6,7]. The negative effects of cold working on the corrosion resistance have been observed in different kinds of stainless steels and considered to be related to dislocation density [8], martensite formation [9], stress [10] and other defects [11]. It seems very hard to balance the mechanical properties and the corrosion resistance of stainless steels. Thus, eliminating the trade-off effect and achieving high-performance HNSs with ultra-high strength and excellent corrosion resistance have great engineering significance.

Wang et al. [12] found that with ultra-high N content (0.98 wt.%), the detrimental effect introduced by cold working in an HNS could be eliminated, and therefore, high mechanical properties and corrosion resistance were achieved. However, it should be pointed out that obtaining ultra-high N content HNSs is very hard due to the low solubility of N [3,13]. Therefore, an alternative approach for improving the pitting corrosion resistance of cold-rolled HNS without additional alloying and sacrificing strength is highly desired.

It is well known that grain-refining is an effective method of improving the hardness and strength of metals and alloys, and ultrafine-grained (UFG) or even nano-grained materials with excellent mechanical properties have already been developed via severe plastic deformation (SPD) methods [14–16]. However, for stainless steels, the effects of grain size on the corrosion resistance are very complicated. As can be seen in Table 1, with grain refinement, the changes in the corrosion resistance of stainless steels are not consistent.

The main difficulties of obtaining high corrosion resistance UFG materials can be attributed to the following factors. The first one is defect density. High-energy zones with a large number of dislocations would result in large pitting formation rate [17]. However, Phadnis et al. [18] reported that with a certain amount of rolling, the diffusion of Cr into the passive film could be enhanced, which resulted in a high repassivation rate. Thus, balancing the harmful and beneficial effects introduced by defect density is the key to improve the comprehensive performance. The second one is grain size distribution. With the same average grain size, the microstructure with uniform grains showed good corrosion resistance in a passivating environment [19]. Gupta and Birbilis [20] reviewed the influence of processing route on the corrosion behavior of nanocrystalline stainless steel, and found that producing a homogenous microstructure is extremely important for improved corrosion resistance. The third one is microstructural stability. Second

* Corresponding authors.
E-mail addresses: pxue@imr.ac.cn (P. Xue), zyma@imr.ac.cn (Z.Y. Ma).

https://doi.org/10.1016/j.corsci.2020.108847
Received 4 November 2019; Received in revised form 13 June 2020; Accepted 1 July 2020
Available online 01 July 2020
0010-938X/ © 2020 Elsevier Ltd. All rights reserved.

Table 1
Effects of grain size on corrosion resistance in previous studies.

Materials	Changes in grain size	Solution	Variation in corrosion resistance with decreased grain size	Ref.
304 stainless steel	50 μm to 80–120 nm	H_2SO_4	Increased	[44]
304 L stainless steel	28 μm to 5 μm	NaCl	Unaffected	[45]
303 stainless steel	20 − 40 μm to 10–20 nm	Borate buffer + 0.1 M NaCl	Decreased	[46]
316 stainless steel	20 μm to 19 nm	NaCl	Decreased	[47]

phase precipitation and grain growth commonly observed in SPD specimens with high stored energy would further influence the corrosion resistance [21]. Therefore, to achieve high strength stainless steels with excellent corrosion resistance, finding an adequate processing method that produces uniform microstructure with high stability is very important.

Friction stir processing (FSP), a variant of friction stir welding, is a very promising SPD method for bulk UFG material production [22]. With additional cooling, uniform ultrafine grains or even nano-scale grains could be achieved via FSP. Compared to other SPD methods, the grain ultra-refinement by FSP did not introduce high density of defects, due to dynamic recrystallization during FSP, producing stable microstructure [23–25]. With these unique features of the FSP materials, the relationship between grain ultra-refinement and corrosion resistance can be more clearly elucidated with significantly minimized influences of other factors.

In this study, we provide a novel method of tailoring the performance of HNSs via FSP. The strength and corrosion resistance of an ultrahigh strength HNS were improved simultaneously by means of grain ultra-refinement. The relationship between grain ultra-refinement and passivation behavior was investigated in detail to further understand the mechanism of property improvement.

2. Experimental

2.1. Materials and processing parameters

2.3 mm Fe-18.4Cr-15.8Mn-2.2Mo-0.66N-0.04C HNS sheets after 50 % cold rolling were used as the base material (BM). Cermet pinless processing tool with a diameter of 10 mm was selected for FSP to reduce the tool damage. In order to obtain UFG microstructure, FSP was conducted at a tool rotation rate of 400 rpm and a welding speed of 25 mm/min, with flowing water cooling.

2.2. Microstructure and mechanical properties

The FSP sample was cut perpendicular to the processing direction for optical microscopy (OM) observation, and the specimen was electrolytically etched in a 10 % oxalic acid solution. The transmission electron microscopy (TEM) specimens were prepared through twin-jet electropolishing with a 10 % perchloric acid and 90 % ethanol solution at − 30 °C. The grain size distribution statistics were made by OM and TEM images, with at least 200 grains being measured. The element distribution and compounds of the passive film were studied by X-ray photoelectron spectroscopy (XPS). HNS was potentiostatically polarized for 1 h to form a stable passive film, and the applied potentials were selected based on the passive region in the polarization curves (0.3 V_{SCE}). To obtain element depth distribution, an Ar-ion beam gun was used during XPS analysis. The scanning transmission electron microscopy (STEM) and energy dispersive X-ray spectroscopy (EDS) analyses were performed by FEI F30 field emission electron microscope.

Vickers hardness tests were performed using a 200 g load for 15 s, at least 5 hardness values were measured. Tensile specimens were cut perpendicular to the processing direction (2.5 mm in gauge length, 1.3 mm in width and 0.7 mm in thickness). Tensile tests were performed at room temperature with a strain rate of 0.001 s^{-1}.

2.3. Corrosion tests and analysis

The immersion test was conducted in a ferric chloride solution to evaluate the pitting corrosion resistance. Following method A in the ASTM G48 standard, specimens were immersed in a 6 % $FeCl_3$ solution, with a temperature of 50 ± 2 °C, for 10 h and 48 h. The corroded specimens were subjected to scanning electron microscopy (SEM) observations.

Electrochemical measurements were performed by using a Gamry Interface 1000 potentiostat/galvanostat at room temperature in a 3.5 % NaCl solution. A three-electrode cell was used with a platinum sheet as the counter electrode and a saturated calomel electrode (SCE) as the reference electrode. Potentiodynamic polarization curves were determined at a scanning rate of 0.5 mV/s. Cyclic polarization curves were recorded from -0.5 V below the open circuit potential with a scan rate of 0.5 mV/s in a 3.5 % NaCl solution. When the anodic current density reached 5 mA/cm^2, the scan was reversed. Before measuring the polarization curves, the specimens were cathodically cleaned at -1.0 V_{SCE} for 180 s.

Furthermore, the repassivation behavior of the BM and FSP samples was investigated via abrading electrode technique. The specimens were abraded mechanically with a 1000 grit SiC disk, and the surface oxide film was removed entirely. With fine grit SiC disk, the effects of surface roughness on the formation of metastable pits can be minimized. The bare surface of the specimens was immersed in a 3.5 % NaCl solution and the current transient curve was recorded. The whole process was carried out in a vacuum environment to prevent oxidation.

3. Results

3.1. Microstructure and mechanical properties

The cross-sectional macrostructure of the FSP sample is shown in Fig. 1(a). As can be clearly observed in Fig. 1(a) and (b), the microstructure of the processed zone (PZ) with a depth of about 0.9 mm was significantly refined, compared to that the BM. Within the grains of the BM, deformation bands with grey contrast were observed (Fig. 1(c)). It should be stressed that the depth and the grain size of the PZ could be controlled via altering the processing parameters, and large area of PZ could be obtained through over-lapping FSP.

From the results of hardness tests in Fig. 2(a), it could be clearly observed that the FSP sample showed higher hardness than the BM. Moreover, as shown in Fig. 2(b), the FSP sample showed ultra-high strength up to 1.7 GPa, much higher than that of the BM (about 1.4 GPa). Obviously, for cold-rolled ultra-high strength HNS, FSP did not sacrifice any hardness or strength.

Fig. 3(a) shows that the microstructure of the cold-rolled HNS was characterized by high density of dislocations and twins, which contributed to high strength of the BM. The formation of twins was attributed to reduced stack fault energy of HNS. After FSP, significant microstructural change occurred. As can be observed in Fig. 3(b) and (c), uniform UFG microstructure was obtained. The defect density in the FSP sample was significantly reduced compared to that in the BM due to dynamic recrystallization. The grain size distribution of the BM and FSP sample are shown in Fig. 3(d) and (e). With the severe deformation and reduced heat-input introduced via water-cooling FSP, the grain size was

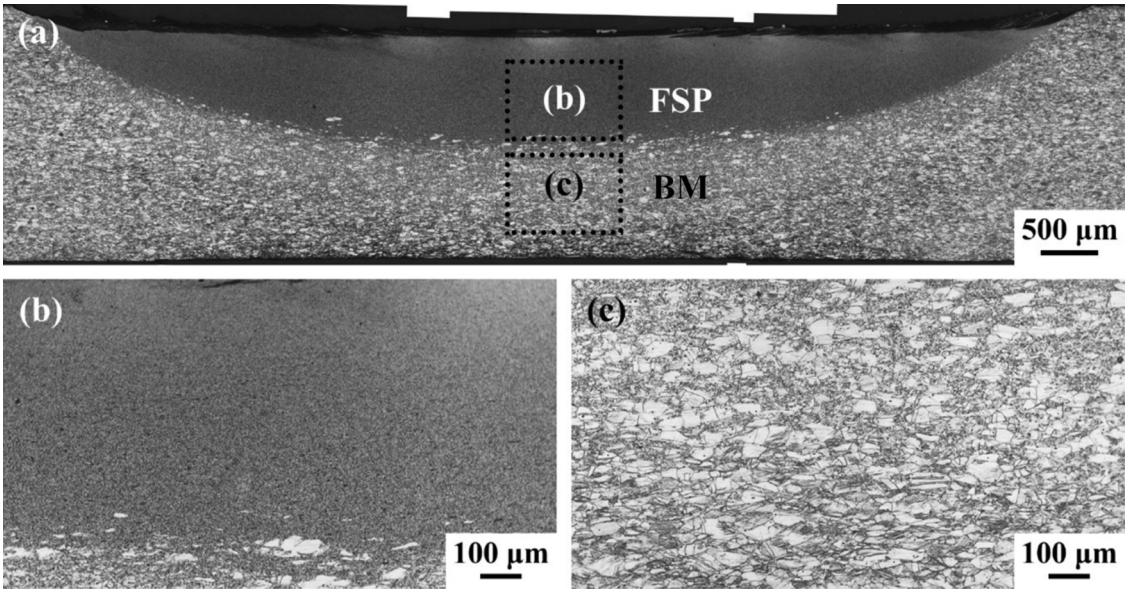

Fig. 1. (a) Cross-sectional macrograph of FSP HNS sample, and microstructure of (b) FSP and (c) BM.

significantly refined from ~37 μm in the BM to ~225 nm in the FSP sample. Thus, the improvement in hardness and strength of the FSP sample should be mainly attributed to the grain ultra-refinement.

3.2. Pitting corrosion behavior of HNS

The surface pitting morphologies after immersed in a $FeCl_3$ solution for 10 and 24 h are shown in Fig. 4. High density of pits were observed on the surface of the BM after 10 h immersion (Fig. 4(a)). However, no large pits could be detected on the surface of the FSP sample (Fig. 4(b)). After immersed for 24 h, the BM was severely corroded, and large pits with a diameter of over 150 μm were clearly observed, as shown in Fig. 4(c). Surprisingly, no large pits could be found on the FSP sample (Fig. 4(d)).

The statistical results of the pit size are shown in Fig. 5. Clearly, the FSP sample exhibited improved pitting resistance, and the pit growth tendency of the FSP sample was also significantly lower than that of the coarse-grained BM. From Figs. 2 and 5, it was very clear that HNS with a UFG microstructure showed an excellent combination of pitting corrosion resistance and mechanical properties.

Fig. 6 shows the cyclic potentiodynamic polarization curves of the BM and FSP samples in a 3.5 % NaCl solution. No significant changes in the corrosion potential (E_{corr}) were observed for both samples, and the BM and FSP samples also showed similar breakdown potentials (0.51 V_{SCE} and 0.49 V_{SCE}, respectively). It is very interesting that, although the forward scan curves were very similar, the reverse scan curves showed major differences. The repassivation potential (E_{rp}) of the BM was about -0.29 V_{SCE}, which was significantly lower than the E_{corr} (-0.17 V_{SCE}), indicating that the pitting nucleation and growth tendency of the BM was very large. In contrast, the FSP sample possessed a much higher E_{rp} (0.02 V_{SCE}), demonstrating that it was much more pitting corrosion resistant. Similar results were also observed for annealed HNS which had similar defect density with the FSP sample (see supplemental files). Clearly, for HNS, the grain size had major influence on the E_{rp}.

4. Discussion

The corrosion behavior of UFG materials is generally affected by four factors, i.e., surface quality, passivation behavior and element distribution of the passive film, precipitation of harmful phases. For the HNS with high microstructural stability in this study, no phase changes after cold rolling or FSP were observed (Fig. 3). Therefore, the corrosion behavior of FSP sample will be discussed from three factors.

4.1. Surface quality

For UFG and nanocrystalline materials produced via SPD method, the surface quality and macro defects have major influences on the corrosion behavior. The formation of crevices and cracks, even with a relatively small size, could seriously deteriorate the corrosion resistance of the samples [26].

As can be seen in Fig. 4(d), even after immersion corrosion for 24 h, the surface of FSP sample was still very smooth, no crevices or microcracks could be observed. This is mainly attributed to the combination of heat-input and forging force during FSP. When the large pressure was applied to the plastic flow metal, crack-free UFG materials could be obtained [22].

4.2. Passivation behavior

The effects of grain boundaries and dislocations on the corrosion behavior of materials are complicated. On one hand, with the increasing defect density, the element diffusion is accelerated in these atom-disorder areas, therefore, repaid passivation can be expected. On

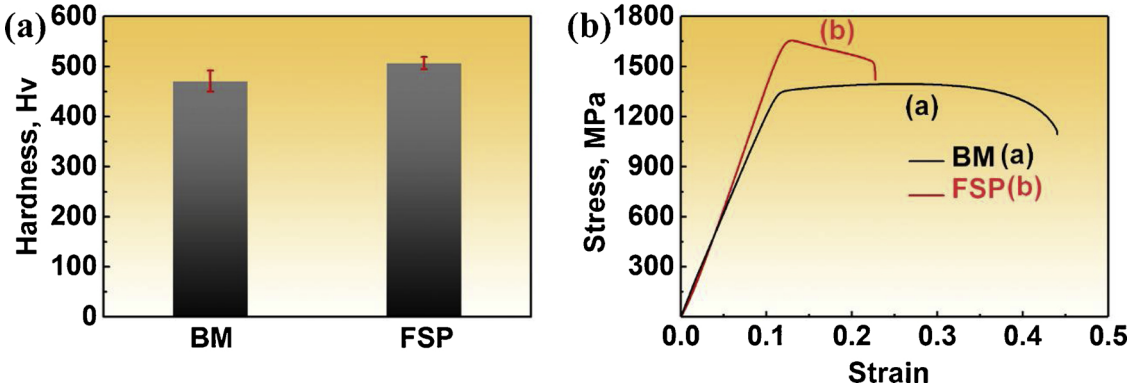

Fig. 2. (a) Vickers hardness and (b) stress-strain curves of BM and FSP samples.

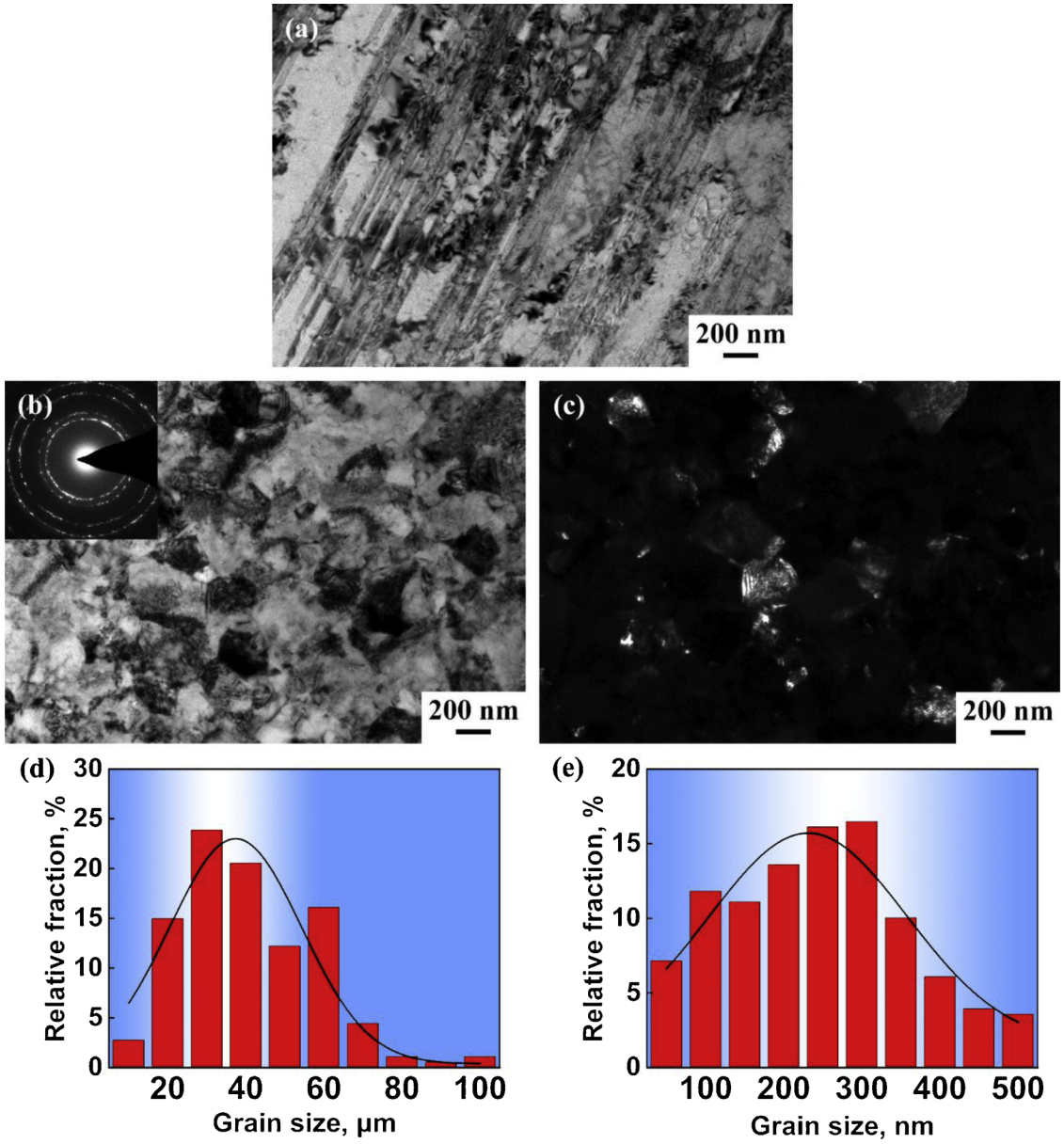

Fig. 3. Microstructure of (a) BM and (b), (c) FSP samples, grain size distribution profiles of (d) BM and (e) FSP samples.

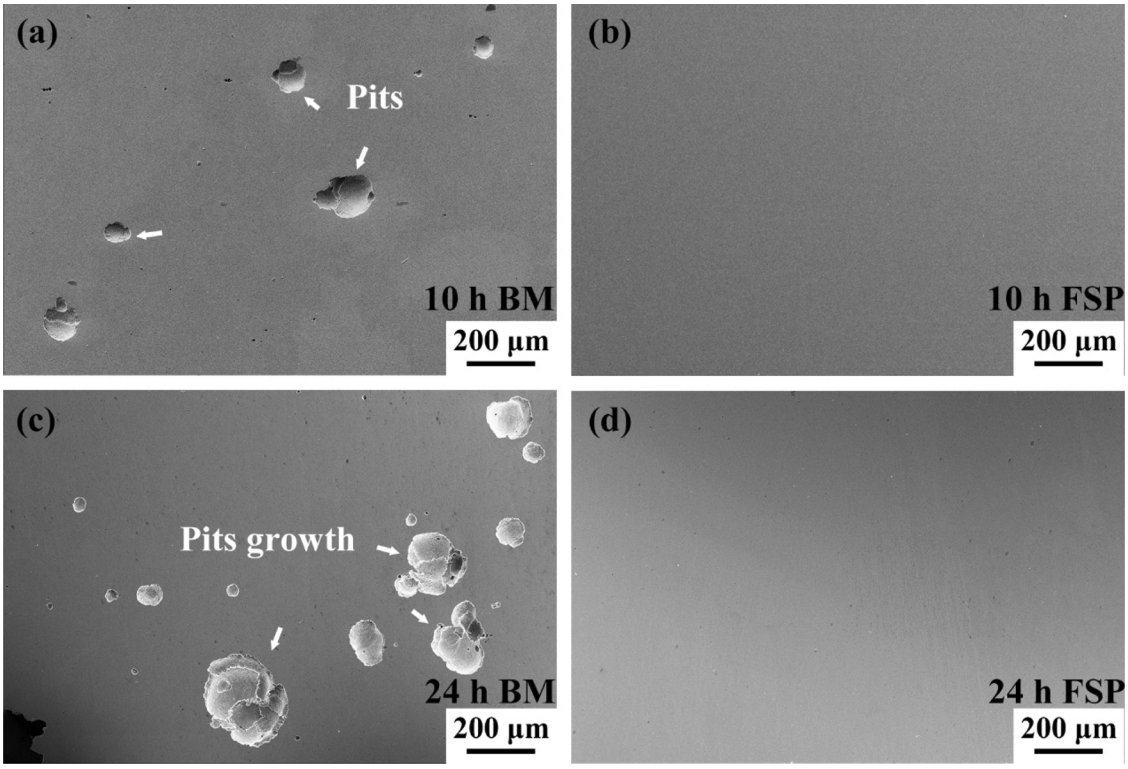

Fig. 4. Pitting morphologies of BM and FSP samples: (a) BM and (b) FSP after immersion for 10 h, (c) BM and (d) FSP after immersion for 24 h.

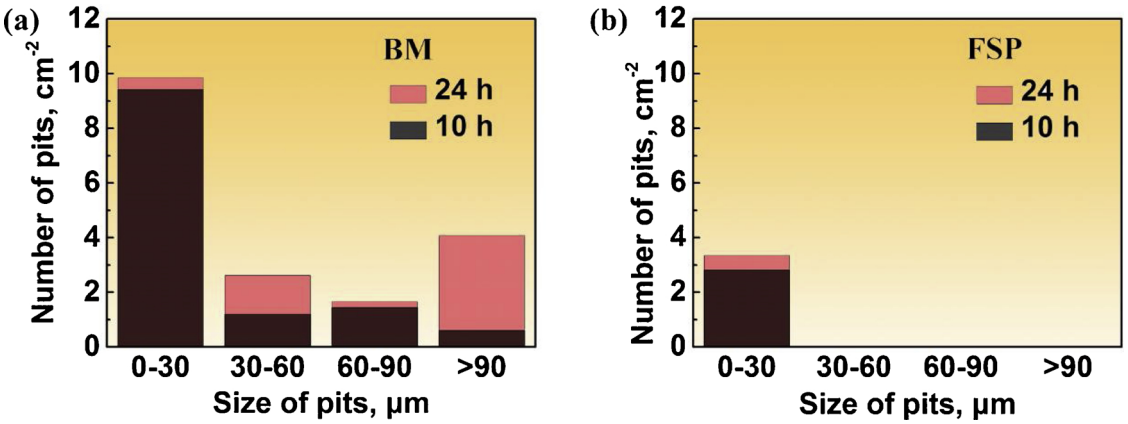

Fig. 5. Statistic pitting distribution of (a) BM and (b) FSP samples for different immersion times.

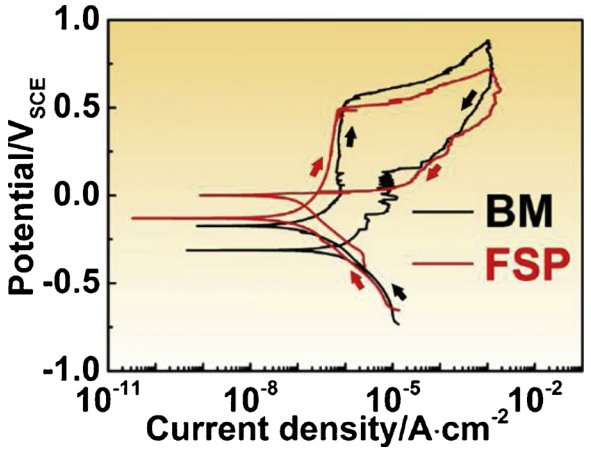

Fig. 6. Cyclic potentiodynamic polarization curves of BM and FSP samples in a 3.5 % NaCl solution.

the other hand, these areas with high energy are also potential pitting sites with reduced barrier energy, therefore, the increased growth rate of the pits can be observed [27]. The competition between these two mechanisms determines the passivation behavior of the material.

Fig. 7 shows the current transient curves obtained by abrading electrode technique. Peak current density was observed when the electrode was immersed in the corrosion medium, and then the current density decreased quickly because of the formation of the passive film. The peak current densities of the BM were much higher than those of the FSP sample under various applied potentials, and it took more time for the BM to achieve a relatively steady current density. Clearly, for 50 % cold-deformed BM, the negative effects of microstructural defects predominated the corrosion behavior.

It has been confirmed that the reaction rate of stainless steels in the electrolytes was very fast in the film formation stage, and the film growth rate is controlled by high field ion conduction [28]. Therefore, the relationship between current density ($i(t)$) and charge flow ($Q(t)$) could be described by the following equation:

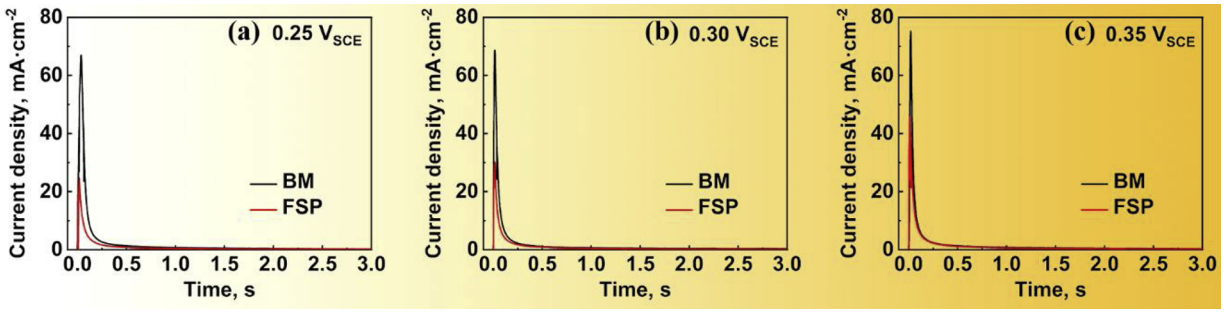

Fig. 7. Current transient curves of BM and FSP samples in a 3.5 % NaCl solution under (a) 0.25 V_{SCE}, (b) 0.30 V_{SCE} and (c) 0.35 V_{SCE}.

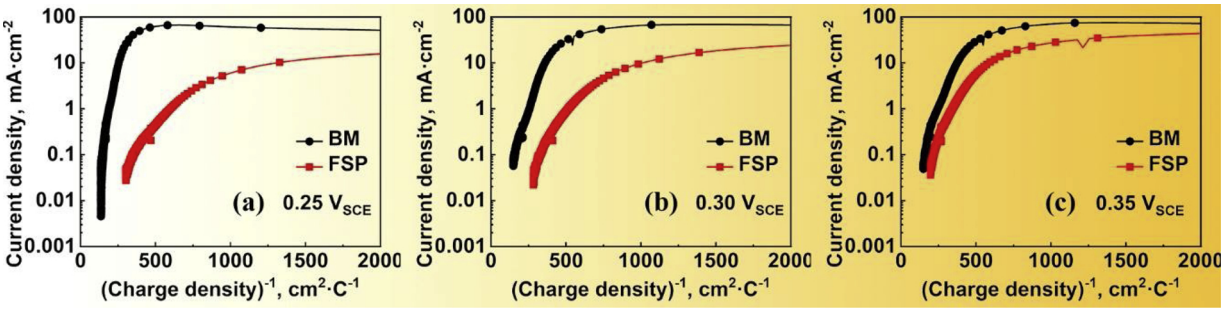

Fig. 8. log$i(t)$ vs. $1/Q(t)$ plots of passive film formed on BM and FSP samples in a 3.5 % NaCl solution under (a) 0.25 V_{SCE}, (b) 0.30 V_{SCE} and (c) 0.35 V_{SCE}.

Table 2
Calculated *cBV* values of passive film on BM and FSP samples.

	0.25 V_{SCE}	0.30 V_{SCE}	0.35 V_{SCE}
BM	1.55E-02 ± 4.95E-5	1.03E-02 ± 4.95E-04	7.79E-03 ± 9.19E-05
FSP	3.23E-03 ± 4.24E-04	4.16E-03 ± 5.30E-04	5.94E-03 ± 9.90E-05

$$\log i(t) = \log A + \frac{cBV}{Q(t)} \quad (1)$$

where A, B and c are constants, V is the potential drop across the film. The cBV value calculated from the log $i(t)$ versus $1/Q(t)$ plot is a very important parameter, and it highly related to the repassivation ability, stress corrosion behavior and the passive film protectiveness of stainless steels [29]. The higher the value of cBV, the lower the repassivation rate, and less protective passive film formed on the surface resulted in higher corrosion susceptibility [30,31].

Fig. 8 shows the log $i(t)$ versus $1/Q(t)$ plots of the BM and FSP samples, and the cBV values were calculated from the slope. As shown in Table 2, the cBV values of the FSP sample were lower than those of the BM at all applied potentials, indicating that the repassivation rate and the passive film protectiveness were enhanced for the FSP sample. The localized dissolution or breakdown of the passive film could be self-repaired efficiently, and consequently the corrosion resistance was improved. As for the BM, an enormous number of deformation bands with high density of dislocations were introduced, these high energy zones not only provided potential pitting sites, but also resulted in low repassivation ability.

4.3. Element distribution

The element distribution and component of the passive film play an extremely important role in repassivation behavior. Fig. 9 shows the XPS results of the passive films after potentiostatically polarized in a 3.5 % NaCl solution at 0.3 V_{SCE} for 1 h. It was seen that the passive film formed on the FSP sample contained a larger content of Cr, Mo and N and a lower content of Fe, therefore exhibited a higher Cr/Fe ratio compared to the BM. The enrichment of elements should be attributed to the higher diffusion rate of elements in the ultrafine-grained microstructure. Numerous results have shown that high Cr/Fe ratio facilitated the repassivation [18,32–34].

Cr is known as one of the most important elements in stainless steels, the formation of Cr_2O_3 is the main reason that makes the steels "stainless". Mo element in the HNSs has two main effects: increasing the solubility of N in the HNSs [13] and strongly inhibiting metastable pitting corrosion [35]. Ilevbare and Burstein [36] found that Mo hindered the nucleation and growth of pits and assisted the repassivation process. The addition of N could accelerate the repassivation rate, leading to an improved corrosion resistance [37].

Fig. 10 is the XPS spectra of the BM and FSP samples. The intensity ratio of Cr-oxide and Cr-hydroxide ($I_{Cr\text{-}ox}/I_{Cr\text{-}hy}$) was 1.84 for the BM and 1.91 for the FSP sample. The presence of more hydroxides in the BM can lead to decreased localized corrosion resistance [27,32]. MoO_3 can absorb the negative charge carriers (O^{2-}) in the passive film and becomes MoO_4^{2-}. The presence of MoO_4^{2-} can neutralize positive donors and inhibits the Cl- absorption, therefore improves the corrosion resistance of steels [38]. Furthermore, the NH_3/NH_4^+ content on the surface of the FSP sample was also higher. It has been well confirmed that NH_3 and NH_4^+ could increase the localized pH value and accelerate the repassivation process [39,40]. The results of XPS agreed very well with the electrochemical tests.

Besides the composition differences in the passive film, some grain boundaries in the BM and FSP samples also showed significant differences in element distribution. From Fig. 11, inhomogeneous element

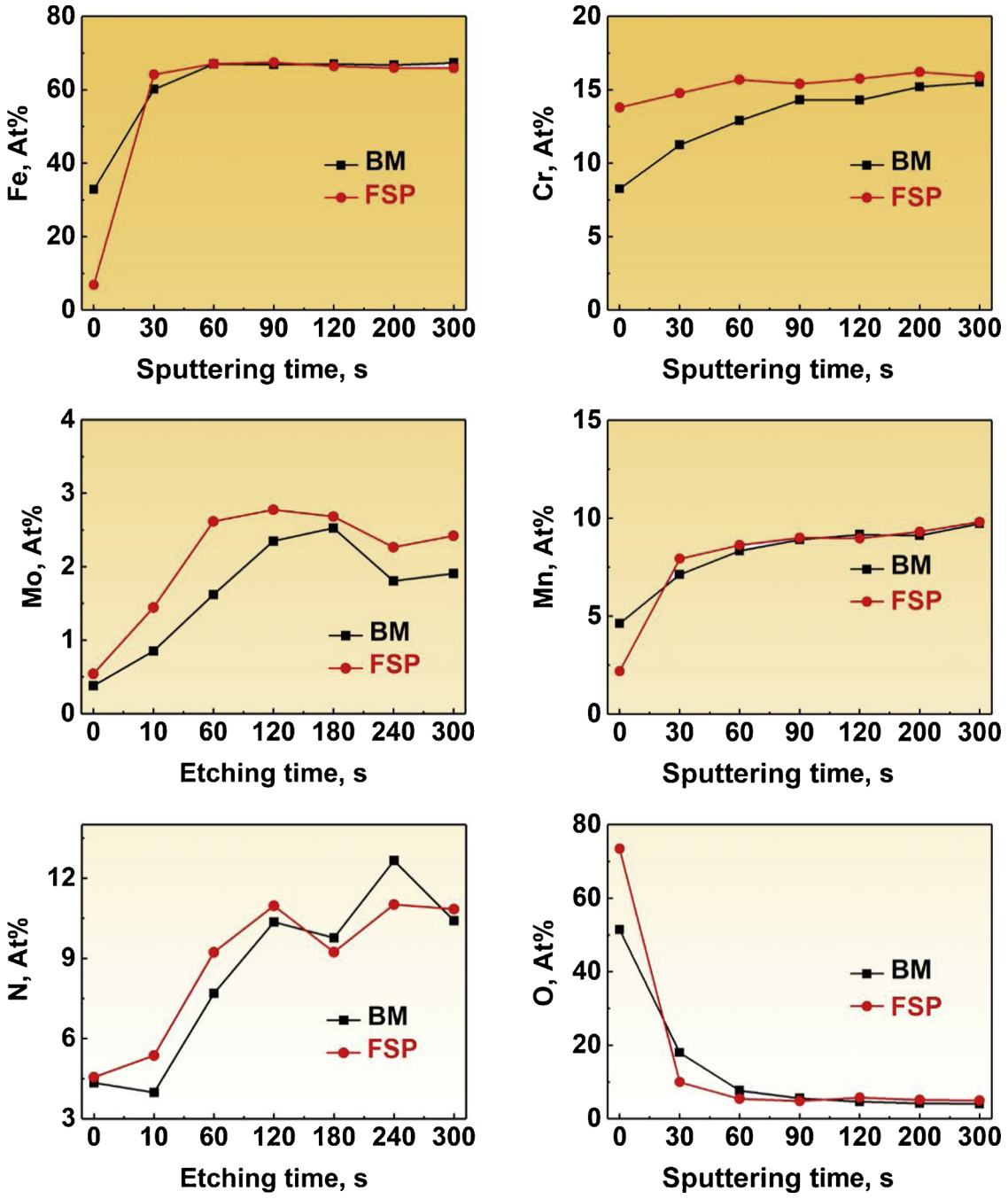

Fig. 9. XPS spectra depth profiles of passive film formed on BM and FSP samples in a 3.5 % NaCl solution.

distribution of Fe, Cr and N could be clearly observed near the grain boundaries of the cold-rolled BM. This phenomenon was also observed in other studies [41,42], and could be explained by the clustering stage before the phase formation.

For the BM, the element depleted zones near the grain boundaries increased the formation frequency of metastable pits and reduced the repassivation ability of passive film. As for the FSP sample, the dynamic recrystallization produced a more homogeneous microstructure including element distribution. The clustering in the BM was redistributed, therefore, no obvious depleted zones were observed near the grain boundaries. As a result, the formation of metastable pits was inhibited (Fig. 7(d)).

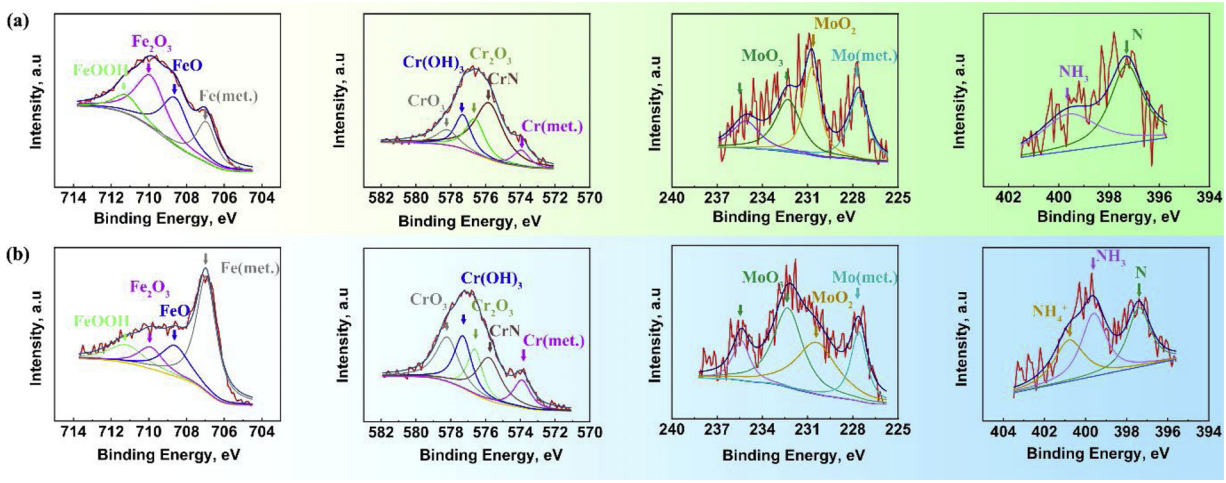

Fig. 10. XPS spectra of main compounds recorded from passive film formed on (a) BM and (b) FSP samples in a 3.5 % NaCl solution.

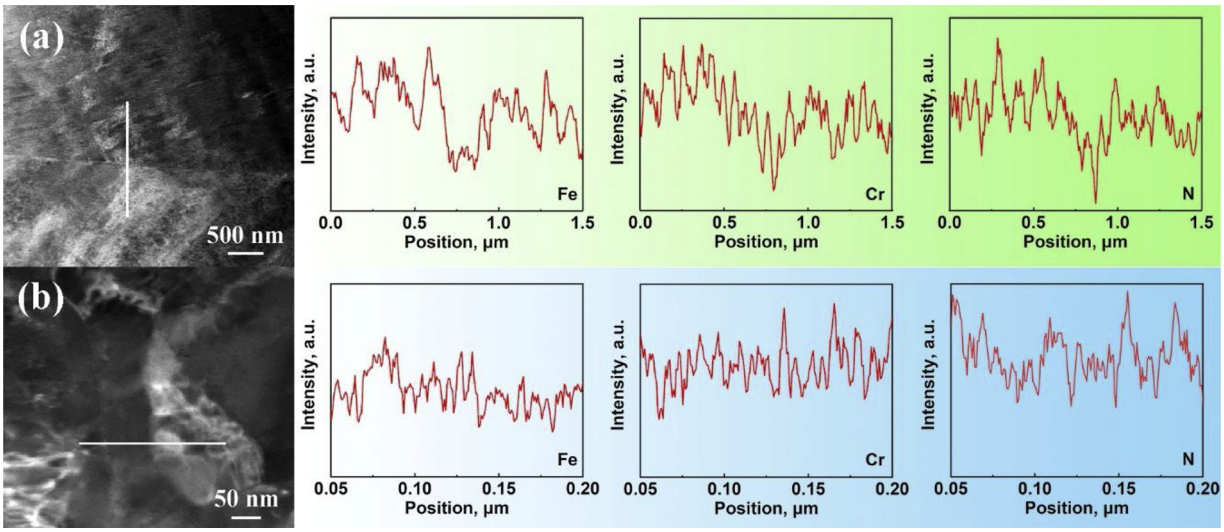

Fig. 11. STEM images and EDS profiles near grain boundaries of (a) BM and (b) FSP samples.

The corrosion behavior of the HNS samples with different grain sizes is illustrated in Fig. 12. The decreased corrosion resistance of the BM is attributed to two factors. With high density of defects and presence of element depleted zones, the formation frequency of metastable pits increases in the BM. Due to the lower Cr, Mo and N content and $I_{Cr\text{-}ox}/I_{Cr\text{-}hy}$ ratio in the passive film, the BM shows inferior repassivation ability. When the passive film breaks down, metastable pits form rapidly, and then metastable pits transform into stable pits quickly and grow at a fast rate.

For the FSP sample, with uniform ultrafine microstructure, homogeneous passive film forms quickly because of the high reaction rate in the electrolytes. The decrease of defect density and redistribution of elements result in significantly less potential pitting sites. With enhanced diffusion rate of element and high content of beneficial elements, the passive film shows improved repassivation ability, metastable pits repassivate rapidly. Moreover, a compact passive film on the FSP sample can prevent Cl^- from penetrating into the substrate and consequently slows down the dissolving rate [43]. Together with the effective strengthening of the UFG microstructure, an ultra-high strength HNS with excellent corrosion resistance was achieved.

5. Conclusions

The pitting corrosion resistance and repassivation behavior of cold-rolled HNS and UFG FSP sample were comparatively studied. With grain ultra-refinement, the mechanical properties and corrosion resistance of the FSP sample were improved simultaneously. The following conclusions are reached:

1 With rapid cooling FSP, the grain size of the processed zone (PZ)

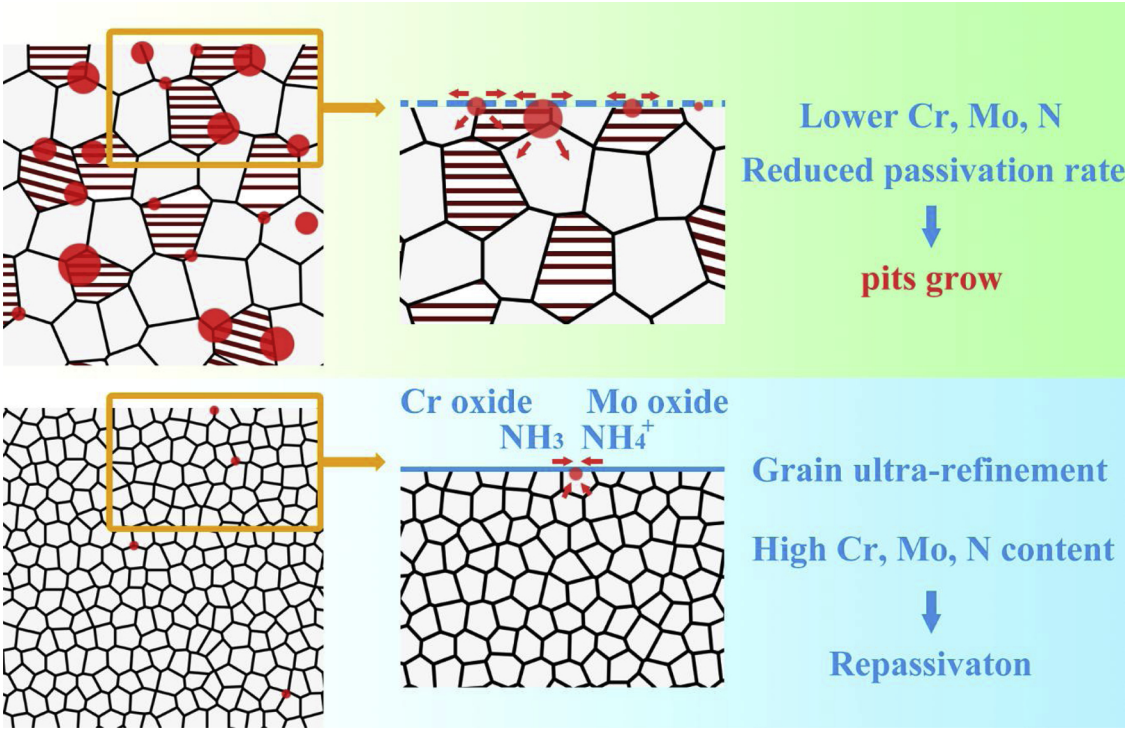

Fig. 12. Corrosion behavior illustration of BM and FSP sample.

was significantly reduced. Uniform ultrafine grains of ~225 nm were achieved in the FSP sample while the grain size of the BM was ~37 μm.

2 The FSP sample showed higher hardness and strength compared with the BM. Ultra-high hardness and strength up to 500 Hv and 1.7 GPa of the FSP sample should be mainly attributed to the UFG microstructure.

3 The FSP sample showed excellent pitting corrosion resistance according to the immersion corrosion test in the $FeCl_3$ solution. The tendency of pit nucleation and growth of the FSP sample was significantly reduced, compared with that of the BM.

4 The grain size had major influences on the repassivation behavior of the HNS. The passive film formed on the FSP sample showed significantly improved repassivation rate and protectiveness due to the high element diffusion rate and element content.

Data availability

The raw/processed data required to reproduce these findings cannot be shared at this time as the data also forms part of an ongoing study.

CRediT authorship contribution statement

H. Zhang: Writing - original draft, Funding acquisition. **P. Xue:** Funding acquisition, Conceptualization. **L.H. Wu:** Investigation, Visualization. **Q.N. Song:** Investigation, Validation. **D. Wang:** Resources, Data curation. **B.L. Xiao:** Methodology, Formal analysis. **Z.Y. Ma:** Writing - review & editing, Supervision.

Declaration of Competing Interest

The authors declare that they have no known competing financial interests or personal relationships that could have appeared to influence the work reported in this paper.

Acknowledgments

This work was supported by the National Natural Science Foundation of China under grant Nos. 51671190 and 51901225, and the Youth Innovation Promotion Association of the Chinese Academy of Sciences (2017236). The authors would like to acknowledge Dr. Y. Cheng (University of Science & Technology Beijing) for kindly performing abrading electrode tests.

Appendix A. Supplementary data

Supplementary material related to this article can be found, in the online version, at doi:https://doi.org/10.1016/j.corsci.2020.108847.

References

[1] W.-C. Jiao, H.-B. Li, J. Dai, H. Feng, Z.-H. Jiang, T. Zhang, D.-K. Xu, H.-C. Zhu, S.-C. Zhang, Effect of partial replacement of carbon by nitrogen on intergranular corrosion behavior of high nitrogen martensitic stainless steels, J. Mater. Sci. Technol. 35 (2019) 2357–2364, https://doi.org/10.1016/j.jmst.2019.06.004.

[2] Z. Wang, Y. Liu, Formation mechanism and application potential of Σ1 boundary in grain boundary engineering of high nitrogen austenitic stainless steel, Mater. Lett. 253 (2019) 377–380, https://doi.org/10.1016/j.matlet.2019.07.011.

[3] J. Li, Q. Wang, Y. Yang, Z. Wu, L. Tan, Y. Ren, K. Yang, Enhancing pitting corrosion resistance of severely cold-worked high nitrogen austenitic stainless steel by nitric acid passivation, J. Electrochem. Soc. 166 (2019) C365–C374, https://doi.org/10.1149/2.0211913jes.

[4] S.C. Sun, G.X. Sun, Z.H. Jiang, C.T. Ji, J.A. Liu, J.S. Lian, Effects of cold rolling deformation on microstructure, hardness, and creep behavior of high nitrogen austenitic stainless steel, Chin. Phys. B 23 (2014) 146–151, https://doi.org/10.1088/1674-1056/23/2/026104.

[5] M. Talha, C.K. Behera, O.P. Sinha, Effect of nitrogen and cold working on structural and mechanical behavior of Ni-free nitrogen containing austenitic stainless steels for biomedical applications, Mater. Sci. Eng. C 47 (2015) 196–203, https://doi.org/10.1016/j.msec.2014.10.078.

[6] Y. Fu, X.Q. Wu, E.H. Han, W. Ke, K. Yang, Z.H. Jiang, Influence of cold work on pitting corrosion behavior of a high nitrogen stainless steel, J. Electrochem. Soc. 155 (2008) C455–C463, https://doi.org/10.1149/1.2939213.

[7] Y. Fu, X. Wu, E.H. Han, W. Ke, K. Yang, Z. Jiang, Effects of cold work and sensitization treatment on the corrosion resistance of high nitrogen stainless steel in chloride solutions, Electrochim. Acta 54 (2009) 1618–1629, https://doi.org/10.1016/j.electacta.2008.09.053.

[8] L. Peguet, B. Malki, B. Baroux, Effect of austenite stability on the pitting corrosion

resistance of cold worked stainless steels, Corros. Sci. 51 (2009) 493–498, https://doi.org/10.1016/j.corsci.2008.12.026.
[9] K. Elayaperumal, P.K. De, J. Balachandra, Passivity of type 304 stainless steel-effect of plastic deformation, Corrosion 28 (1972) 269–273, https://doi.org/10.5006/0010-9312-28.7.269.
[10] B. Ravi Kumar, B. Mahato, R. Singh, Influence of cold-worked structure on electrochemical properties of austenitic stainless steels, Metall. Mater. Trans. A Phys. Metall. Mater. Sci. 38 (A) (2007) 2085–2094, https://doi.org/10.1007/s11661-007-9224-4.
[11] K. Arioka, T. Yamada, T. Miyamoto, T. Terachi, Dependence of stress corrosion cracking of alloy 690 on temperature, cold work, and carbide precipitation—role of diffusion of vacancies at crack tips, Corrosion 67 (2011) 35001–35006, https://doi.org/10.5006/1.3563640.
[12] Q. Wang, B. Zhang, Y. Ren, K. Yang, Eliminating detrimental effect of cold working on pitting corrosion resistance in high nitrogen austenitic stainless steels, Corros. Sci. 123 (2017) 351–355, https://doi.org/10.1016/j.corsci.2017.04.006.
[13] J.W. Simmons, Overview: High-nitrogen alloying of stainless steels, Mater. Sci. Eng. A 207 (1996) 159–169, https://doi.org/10.1016/0921-5093(95)09991-3.
[14] Q. Wei, H.T. Zhang, B.E. Schuster, K.T. Ramesh, R.Z. Valiev, L.J. Kecskes, R.J. Dowding, L. Magness, K. Cho, Microstructure and mechanical properties of super-strong nanocrystalline tungsten processed by high-pressure torsion, Acta Mater. 54 (2006) 4079–4089, https://doi.org/10.1016/j.actamat.2006.05.005.
[15] F.Y. Dong, P. Zhang, J.C. Pang, Q.Q. Duan, Y. Bin Ren, K. Yang, Z.F. Zhang, Microstructure and mechanical properties of high-nitrogen austenitic stainless steels subjected to equal-channel angular pressing, Acta Metall. Sin. Engl. Lett. 29 (2016) 140–149, https://doi.org/10.1007/s40195-016-0370-9.
[16] S.-H. Lee, H. Utsunomiya, T. Sakai, Microstructures and mechanical properties of ultra low carbon interstitial free steel severely deformed by a multi-stack accumulative roll bonding process, Mater. Trans. 45 (2005) 2177–2181, https://doi.org/10.2320/matertrans.45.2177.
[17] S.K. Pradhan, P. Bhuyan, S. Mandal, Influence of the individual microstructural features on pitting corrosion in type 304 austenitic stainless steel, Corros. Sci. 158 (2019) 108091, , https://doi.org/10.1016/j.corsci.2019.108091.
[18] S.V. Phadnis, A.K. Satpati, K.P. Muthe, J.C. Vyas, R.I. Sundaresan, Comparison of rolled and heat treated SS304 in chloride solution using electrochemical and XPS techniques, Corros. Sci. 45 (2003) 2467–2483, https://doi.org/10.1016/S0010-938X(03)00099-4.
[19] S. Gollapudi, Grain size distribution effects on the corrosion behaviour of materials, Corros. Sci. 62 (2012) 90–94, https://doi.org/10.1016/j.corsci.2012.04.040.
[20] R.K. Gupta, N. Birbilis, The influence of nanocrystalline structure and processing route on corrosion of stainless steel: a review, Corros. Sci. 92 (2015) 1–15, https://doi.org/10.1016/j.corsci.2014.11.041.
[21] H.-S. Cho, K. Lee, Effect of cold working and isothermal aging on the precipitation of sigma phase in 2205 duplex stainless steel, Mater. Charact. 75 (2013) 29–34, https://doi.org/10.1016/j.matchar.2012.10.006.
[22] P. Xue, Z. Huang, B. Wang, Y. Tian, W. Wang, B. Xiao, Z. Ma, Intrinsic high cycle fatigue behavior of ultrafine grained pure Cu with stable structure, Sci. China Mater. 59 (2016) 531–537, https://doi.org/10.1007/s40843-016-5068-6.
[23] Z.Y. Ma, Friction stir processing technology: a review, Metall. Mater. Trans. A Phys. Metall. Mater. Sci. 39 (A) (2008) 642–658, https://doi.org/10.1007/s11661-007-9459-0.
[24] P. Xue, B.L. Xiao, Z.Y. Ma, Enhanced strength and ductility of friction stir processed Cu-Al alloys with abundant twin boundaries, Scr. Mater. 68 (2013) 751–754, https://doi.org/10.1016/j.scriptamat.2013.01.003.
[25] S. Sabooni, F. Karimzadeh, M.H. Enayati, A.H.W. Ngan, Friction-stir welding of ultrafine grained austenitic 304L stainless steel produced by martensitic thermo-mechanical processing, Mater. Des. 76 (2015) 130–140, https://doi.org/10.1016/j.matdes.2015.03.052.
[26] Y. wei Hao, B. Deng, C. Zhong, Y. ming Jiang, J. Li, Effect of surface mechanical attrition treatment on corrosion behavior of 316 stainless steel, J. Iron Steel Res. Int. 16 (2009) 68–72, https://doi.org/10.1016/S1006-706X(09)60030-3.
[27] Y. Fu, X. Wu, E.H. Han, W. Ke, K. Yang, Z. Jiang, Effects of nitrogen on the passivation of nickel-free high nitrogen and manganese stainless steels in acidic chloride solutions, Electrochim. Acta 54 (2009) 4005–4014, https://doi.org/10.1016/j.electacta.2009.02.024.
[28] G.T. Burstein, P.I. Marshall, Growth of passivating films on scratched 304L stainless steel in alkaline solution, Corros. Sci. 23 (1983) 125–137, https://doi.org/10.1016/0010-938X(83)90111-7.
[29] E.A. Cho, C.K. Kim, J.S. Kim, H.S. Kwon, Quantitative analysis of repassivation kinetics of ferritic stainless steels based on the high field ion conduction model, Electrochim. Acta 45 (2000) 1933–1942, https://doi.org/10.1016/S0013-4686(99)00415-6.
[30] I.U.H. Toor, K.J. Park, H. Kwon, Manganese effects on repassivation kinetics and SCC susceptibility of high Mn-N austenitic stainless steel alloys, J. Electrochem. Soc. 154 (2007) 494–499, https://doi.org/10.1149/1.2752089.
[31] J. Wang, X. Li, J. Wang, E. hou Han, Development of a scratch electrode system in high temperature high pressure water, Corros. Sci. 95 (2015) 125–132, https://doi.org/10.1016/j.corsci.2015.03.006.
[32] H. Luo, Q. Yu, C. Dong, G. Sha, Z. Liu, J. Liang, L. Wang, G. Han, X. Li, Influence of the aging time on the microstructure and electrochemical behaviour of a 15-5PH ultra-high strength stainless steel, Corros. Sci. 139 (2018) 185–196, https://doi.org/10.1016/j.corsci.2018.04.032.
[33] M.P. Ryan, D.E. Williams, R.J. Chater, B.M. Hutton, D.S. McPhail, Why stainless steel corrodes, Nature 415 (2002) 770–774, https://doi.org/10.1038/415770a.
[34] R. Devaux, D. Vouagner, A.M. de Becdelievre, C. Duret-Thual, Electrochemical and surface studies of the ageing of passive layers grown on stainless steel in neutral chloride solution, Corros. Sci. 36 (1994) 171–186, https://doi.org/10.1016/0010-938X(94)90118-X.
[35] W.J. Tobler, S. Virtanen, Effect of Mo species on metastable pitting of Fe18Cr alloys-A current transient analysis, Corros. Sci. 48 (2006) 1585–1607, https://doi.org/10.1016/j.corsci.2005.05.049.
[36] G.O. Ilevbare, G.T. Burstein, Role of alloyed molybdenum in the inhibition of pitting corrosion in stainless steels, Corros. Sci. 43 (2001) 485–513, https://doi.org/10.1016/S0010-938X(00)00086-X.
[37] J.W. Park, V.S. Rao, H.S. Kwon, Effects of nitrogen on the repassivation behavior of Type 304L stainless steel in chloride solution, Corrosion 60 (2004) 1099–1103, https://doi.org/10.5006/1.3299223.
[38] A. Irhzo, Y. Segui, N. Bui, F. Dabosi, On the conduction mechanisms of passive films on molybdenum-containing stainless steel, Corrosion 42 (1986) 141–147, https://doi.org/10.5006/1.3584893.
[39] M.K. Lei, X.M. Zhu, Role of nitrogen in pitting corrosion resistance of a high-nitrogen face-centered-cubic phase formed on austenitic stainless steel, J. Electrochem. Soc. 152 (2005) B291, https://doi.org/10.1149/1.1939245.
[40] F.M. Bayoumi, W.A. Ghanem, Effect of nitrogen on the corrosion behavior of austenitic stainless steel in chloride solutions, Mater. Lett. 59 (2005) 3311–3314, https://doi.org/10.1016/j.matlet.2005.05.063.
[41] F. Danoix, P. Auger, Atom probe studies of the Fe-Cr system and stainless steels aged at intermediate temperature: a review, Mater. Charact. 44 (2000) 177–201, https://doi.org/10.1016/S1044-5803(99)00048-0.
[42] X. Zhou, X.X. Yu, T. Kaub, R.L. Martens, G.B. Thompson, Grain boundary specific segregation in nanocrystalline Fe(Cr), Sci. Rep. 6 (2016) 1–14, https://doi.org/10.1038/srep34642.
[43] W. Ye, Y. Li, F. Wang, Effects of nanocrystallization on the corrosion behavior of 309 stainless steel, Electrochim. Acta 51 (2006) 4426–4432, https://doi.org/10.1016/j.electacta.2005.12.034.
[44] Z.J. Zheng, Y. Gao, Y. Gui, M. Zhu, Corrosion behaviour of nanocrystalline 304 stainless steel prepared by equal channel angular pressing, Corros. Sci. 54 (2012) 60–67, https://doi.org/10.1016/j.corsci.2011.08.049.
[45] A. Abbasi Aghuy, M. Zakeri, M.H. Moayed, M. Mazinani, Effect of grain size on pitting corrosion of 304L austenitic stainless steel, Corros. Sci. 94 (2015) 368–376, https://doi.org/10.1016/j.corsci.2015.02.024.
[46] M. Pisarek, P. Kędzierzawski, M. Janik-Czachor, K.J. Kurzydłowski, Effect of hydrostatic extrusion on passivity breakdown on 303 austenitic stainless steel in chloride solution, J. Solid State Electrochem. 13 (2009) 283–291, https://doi.org/10.1007/s10008-007-0488-9.
[47] Y. wei Hao, B. Deng, C. Zhong, Y. ming Jiang, J. Li, Effect of surface mechanical attrition treatment on corrosion behavior of 316 stainless steel, J. Iron Steel Res. Int. 16 (2009) 68–72, https://doi.org/10.1016/S1006-706X(09)60030-3.